Determination of a cohesive law for delamination modelling - Accounting for variation in crack opening and stress state across the test specimen width

Joki, R. K.; Grytten, F.; Hayman, Brian; Sørensen, Bent F.

Published in:
Composites Science and Technology

Link to article, DOI:
10.1016/j.compscitech.2016.01.026

Publication date:
2016

Document Version
Peer reviewed version

Determination of a Cohesive Law for Delamination Modelling – Accounting for Variation in Crack Opening and Stress State Across the Test Specimen Width

R. K. Joki*[a,b], F. Grytten[c] , B. Hayman[b], B. F. Sørensen[d]

[a] FiReCo AS, Storgata 15, 1607 Fredrikstad, Norway
[b] University of Oslo, Department of Mathematics, Pb 1053 Blindern, 0316 OSLO, Norway
[c] SINTEF MC, Department of Materials and nanotechnology, Pb. 124 Blindern, 0314 Oslo, Norway
[d] Technical University of Denmark, Department of Wind Energy, Frederiksborgvej 399, 4000 Roskilde, Denmark

*Corresponding author. Tel.: +47 909 13 046

E-mail addresses: Reidar.joki@fireco.no (R. K. Joki), Frode.Grytten@sintef.no (F. Grytten), brianha@math.uio.no (B. Hayman), bsqr@dtu.dk (B. F. Sørensen).

Abstract

The cohesive law for Mode I delamination in glass fibre Non-Crimped Fabric reinforced vinylester is determined for use in finite element models. The cohesive law is derived from a delamination test based on DCB specimens loaded with pure bending moments taking into account the presence of large-scale bridging and the multi-axial state of stress in the test specimen. The fracture resistance is calculated from the applied moments, the elastic material properties and the geometry of the test specimen. The cohesive law is then determined in a three step procedure: 1) Obtain the bridging law by differentiating the fracture resistance with respect to opening displacement at the initial location of the crack tip, measured at the specimen edge. 2) Extend the bridging law to a cohesive law by accounting for crack tip fracture energy. 3) Fine-tune the cohesive law through an iterative modelling approach so that the changing state of stress and deformation across the width of the test specimen is taken into account. The changing state of stress and deformation across the specimen width is shown to be significant for small openings (small fracture process zone size). This will also be important for the initial part of the cohesive law with high stress variation for small openings (a few microns), but the effects are expected to be smaller for large-scale-bridging where the stress varies slowly over an increase in crack opening of several millimetres. The accuracy of the proposed approach is assessed by comparing the results of numerical simulation using the cohesive law derived by the above method, with those of physical testing for the standard DCB Mode I delamination test (ASTM D 5528).

Key words: Polymer-matrix composites (PMCs); Delamination; Finite element analysis (FEA)

1 Introduction

The fracture process zone (FPZ) in a delaminating fibre reinforced polymer laminate is usually long in the plane of fracture in comparison with the smallest specimen dimension, i.e. the thickness of the laminate. The reason for the large FPZ is the development of fibre bridging following in the wake of the crack tip. Fibre bridging is beneficial in the sense that it leads to an increased fracture resistance, and thus increases the damage tolerance. Cohesive zone models (CZM) [1, 2] are well suited for modelling this kind of FPZ. A CZM can be implemented by inserting cohesive elements [3] at interfaces where fracture is expected to propagate. Therefore CZM has become a favoured tool for modelling delamination [4-17]. A cohesive law that relates separation of the fracturing surfaces to the traction transferred between them governs the cohesive elements. Since the law relates tractions to separation, it is often referred to as a traction-separation law. A major challenge in the use of CZM in structural design of engineering structures is to characterise the cohesive law of the real fracture process zone of the material or interface. The existing test standards [18, 19] concerned with interface properties of fibre reinforced polymer composites are designed for determining the critical energy release rate, i.e. under the premises of linear-elastic fracture mechanics (small-scale fracture process zone). Within linear-elastic fracture mechanics, the criterion for crack growth is that the energy release rate is equal to the work per unit area of the cohesive tractions and represents the fracture energy associated with a fully developed FPZ [20, 21]. However, linear-elastic fracture mechanics concepts are not applicable for large-scale bridging problems; instead cohesive laws can be used for representing the mechanics of fracture, including the energy dissipation at a crack tip and the work of tractions in a bridging zone behind the crack tip. Crack initiation and arrest, and thus the shape of the delaminated area in a composite structure are governed not only by the overall geometry, the loading and the total fracture resistance but also by underlying details of the traction-separation law [22]. More reliable procedures for determining the underlying details of the traction-separation law are needed.

The path independent J integral [20] has been adopted to determine the cohesive laws from experiments [12-14, 23] for plane problems. This has opened for the possibility of measuring the shape of the cohesive law. For large-scale bridging (LSB) problems, the J integral of the standard DCB specimen loaded with wedge forces can be determined experimentally by measuring the rotations where the forces are applied [24, 25], i.e. requiring more

instrumentation than for the LEFM delamination test. Although with the *J* integral approach more instrumentation is needed in a DCB configuration, there is no need to monitor the crack tip position during the test, which is always difficult. The need to measure rotations can be avoided by applying pure bending moments to the test specimens instead of forces [17, 21], since for the DCB loaded with pure bending moments the *J* integral is given in closed analytical form, independent of crack length and valid also for LSB-problems. In reality, 3-dimensional (3D) effects associated with anticlastic bending [26] of the beams in the cracked region lead to inaccuracy when the crack opening is measured at the edge of the specimen; the anticlastic curvature makes the crack opening at the edge of the specimen smaller than that at mid-width, while restraint of the anticlastic bending in the middle region induces variation of the stress state across the specimen width. These effects also cause the longitudinal position of the crack tip to vary across the width of a fracture mechanics test specimen. Then the resulting cohesive tractions will vary across the specimen, in particular in the representation of the crack tip fracture energy, where the cohesive traction is expected to vary from high to near-zero over small openings.

A remaining challenge is to extend the approach for plane problems to 3-dimensional problems and account for the changing state of stress across the width of the specimen. As will be shown later, both material properties and specimen geometry affect the result.

The objective of the present study is to demonstrate that a cohesive law for 3D finite element implementation can be fitted from experimental test results taking into account the changing crack opening and state of stress across the width of the test specimen. In the study, DCB tests using pure bending moments have been carried out on a set of laminate specimens. Attempts have then been made to derive from these tests a cohesive law for Mode I delamination using a modified iterative modelling approach [27-30]. First, the cohesive law for Mode I delamination is obtained using the *J* integral approach for plane problems [12], which implicitly assumes that the crack opening is the same across the width of the specimen. A simplified, multi-linear cohesive law is then implemented in a three-dimensional finite element model where the parameters describing the cohesive law are defined as variables. These variables are then optimised for the model result to fit the experimental response. The variation in crack opening across the test specimen is then accounted for. Finally, the accuracy of the approach is tested by numerically simulating a separate test, namely the

standardised ASTM double cantilever beam (DCB) specimen [18], using the derived cohesive law, and comparing the calculated load-displacement response to that from a corresponding physical test. Note that the standardised DCB specimens and the moment loaded DCB specimens had different widths and width to height ratios.

A short theoretical background for the use of the *J* integral and the effect of changing state of stress is presented in the following section.

2 The path independent J integral approach

The path independent *J* integral was first applied to crack problems by Rice [20] and can be used to calculate the fracture resistance, J_R , during crack growth.

For a homogeneous DCB specimen loaded by pure bending moments, an evaluation of the *J* integral along the external boundaries of the DCB specimen in Figure 1 c) gives (assuming plane stress) [31]

$$J_{R,ext} = \frac{12M^2}{B^2H^3E_{11}}, \tag{1}$$

where *M* is the applied moment, *B* and *H* are the beam width and height, respectively and E_{11} is the Young's modulus in the x_1 direction. In the present paper, the composite laminates are analysed as homogeneous beams. This is assumed to be acceptable provided the correct bending stiffness is modelled.

Evaluating the *J* integral along the edge of the FPZ in Figure 1 a) gives [20, 31]

$$J_{R,FPZ} = \int_0^{\delta^*} \sigma_{FB}(\delta)\,\mathrm{d}\delta + J_{tip}, \tag{2}$$

where δ^* is the end-opening of the FPZ, $\sigma_{FB}(\delta)$ is the traction as a function of separation δ along the FPZ associated with fibre bridging and J_{tip} is the *J* integral evaluated around the crack tip.

Due to path-independence, $J_{R,ext} = J_{R,FPZ}$. At low load levels when $J_{R,ext}$ (or equivalently, $J_{R,FPZ}$) is below a certain value, denoted J_0 , no crack growth takes place and $\delta^* = 0$. When the external load is increased so that $J_{R,ext}$ reaches J_0 , the crack will open ($\delta^* > 0$). J_0 is thus the

crack tip fracture energy. A bridging zone now forms between the initial and the present crack tip. The length of the bridging zone is denoted L. With increasing $J_{R,ext}$, the length of the active cohesive zone, L, and the end-opening, δ^*, increase as the crack tip advances. When δ^* reaches a critical value, δ_0, the fracture surfaces are completely separated at the end of the crack. The FPZ is then fully developed and the fracture resistance attains a constant value, denoted the steady-state fracture resistance, which represents work of separation per unit area of the cohesive traction. For steady-state specimens, further crack extension will not cause an increase in the active cohesive zone length, L, while for other fracture specimens, the active cohesive zone length may continue to change [30].

In equation (2), the traction-separation law represents a bridging law describing the relation between traction and separation in the wake of the crack tip. When the FPZ is modelled using cohesive elements the crack tip energy is included in the traction separation law and equation (2) becomes [13]

$$J_{R,FPZ} = \int_0^{\delta^*} \sigma_{CL}(\delta)\,\mathrm{d}\delta, \tag{3}$$

where $\sigma_{CL}(\delta)$ represents the cohesive law.

The relation between the tractions and the opening separation at the crack end can then be obtained by differentiating the external J integral with respect to the end opening of the cohesive zone [23, 31]. By assuming this is representative for the rest of the interface, the cohesive law for the interfaces is given:

$$\sigma_{CL}(\delta^*) = \frac{\partial J_{R,ext}}{\partial \delta^*} \tag{4}$$

In equation (4), $\sigma_{CL}(\delta^*)$ can be understood as the traction acting at the position of the end opening of the cohesive zone. However, assuming the cohesive law is a material property, independent of position, the general cohesive law is the same as the one found at the end-opening, so that in the functional form for the cohesive law we can replace δ^* with δ.

3 Test specimen, experimental setup, data analysis and results

The mechanical properties of the non-crimp fabric glass-fibre vinylester composite material and dimensions of the DCB test samples are presented in Table 1 and illustrated in Figure 2. The lay-up is $[(90/0)_9]_S$, and the weight distribution within each ply is 95% in the 0° direction and 5% in the 90° direction, so that the laminate does not possess bend-twist coupling. The

end-opening δ^* was measured using an extensometer attached to the side of the upper and lower beams at the initial prefabricated crack tip at $(x_1, x_2) = (0, \pm H/2)$. Mode I delamination was promoted by applying equal moments in the opposite directions in a progressive manner by increasing the rotations of the specimen beam ends [17]. The fracture resistance was calculated from the measured applied moments, equation (1).

An exponential decay function of the following form was fitted to the fracture resistance:

$$J_R(\delta) = J_a\left(1 - e^{-\delta/\delta_a}\right) + J_b\left(1 - e^{-\delta/\delta_b}\right) + J_0 \quad (5)$$

where the fitting parameters J_a, δ_a, J_b and δ_b are presented in Table 1. The resulting fracture resistance curves are plotted in Figure 3 a). In Figure 3 b) it can be seen that the fracture resistance increases before any opening displacement is observed. The fracture resistance at which the opening displacement starts is associated with the crack tip fracture energy, J_0. The crack tip fracture energy is the base for the fitted function plotted in Figure 3 a) and b). A bridging law is obtained by differentiating the fitted function analytically with respect to the end-opening in accordance with equation (4). The result is (see Figure 3 c):

$$\sigma_{FB} = \delta_a J_a e^{-\delta/\delta_a} + \delta_b J_b e^{-\delta/\delta_b} \quad (6)$$

The derived bridging law is highly non-linear. The peak stress is approximately 0.9 MPa and the critical separation, δ_0 is about 3 mm. The bridging law does not include the deformations (separation) associated with the crack tip that gives rise to J_0, see equation (2). As seen in Figure 3 b), J_0 is dissipated within a small opening displacement (assumed to be in the order of 0.01 mm).

A cohesive law should prescribe a traction-separation relation that dissipates the total energy associated with both the cracking at the crack tip and fibre bridging in the bridging zone. Figure 3 d) presents a cohesive law that has a cohesive traction that increases to a peak value, $\hat{\sigma}$, stays constant for a small opening, $\hat{\delta}$, and then decays rapidly within small openings added to the initial part of the bridging law such that the cohesive law includes work of cohesive tractions corresponding to the crack tip fracture energy. The value of $\hat{\sigma}$ represents the interface strength and $\hat{\delta}$ needs to be fitted so the area under the traction-separation law equals the critical crack tip energy. In reality only J_0, determined by acoustic emission and initiation of crack end opening, can be determined from experiments; the chosen peak stress

therefore affects the associated separations and vice versa. Accurate determination of the peak stress and separation parameters is a key issue in the remainder of this paper.

It is well known that for wide specimens the crack front often has a "thumb-nail" shape, i.e. the crack is somewhat shorter at the free edges and longest half way across the specimen width [32]. The opening displacement at a given x_1 position within the active cohesive zone is thus not constant across the specimen width.

Therefore, the opening displacement δ^* measured at the side of the specimen does not accurately represent the behaviour for the whole delamination front. Furthermore, partial restriction of anticlastic bending leads to deviation from a state of plane stress. Consequently, the interface traction obtained with the plane stress assumption through equation (4) will not be accurate. In the next section it will be shown that the opening tractions are non-uniform across the specimen width and that the non-uniformity is affected by the Poisson's ratio. This is of particular importance for small openings where the value of the cohesive traction is expected to vary significantly, such as in the description of cohesive laws representing the crack tip fracture energy J_0.

4 Numerical approach and results

A three-dimensional finite element model of the DCB specimen was made using the LS-DYNA finite element code. The specimen material and geometric properties are presented in Table 1 and Figure 2. The beams in the moment loaded DCB specimen were modelled using 8-node solid elements with an isotropic material description fitted to resemble the flexural stiffness of the composite beams. The beams were modelled using volume elements with all sides having lengths of approximately 0.5 mm. An orthotropic material description with a full lay-up description based on unidirectional plies did not produce significantly different results from an isotropic one as long at the bending stiffness was unchanged. Due to symmetry, only one-half of the width of the specimen was modelled. The model is illustrated in Figure 4. The surfaces at the beam-ends in Figure 4 are modelled as rigid bodies. The simulations were executed in a nonlinear dynamic analysis with implicit time integration. The reason for using a dynamic analysis was to introduce the mass-matrix to ease the convergence in each load step. Monotonically increasing equal moments, acting in opposite directions, are prescribed to

these rigid bodies. The contact area between fixture and beam is the same as in the experiments [17].

The fracture interface was modelled with 8-noded finite-thickness cohesive elements with a general cohesive material formulation referred to as *MAT_186 in the LS-DYNA material library [33]. The cohesive elements had the dimensions: 0.5 mm, 0.5 mm, and 0.001 mm in width, length and thickness respectively. The constitutive model is a cohesive law that includes both crack tip and fibre bridging behaviour.

As a preliminary investigation, to evaluate the effect of the above mentioned stress and crack opening variations across the width [32], a simple bi-linear cohesive law was used as model input. The cohesive law parameters are given in terms of the peak stress (set to 20 MPa) and the critical separation, δ_0, was set to 0.1 mm. These parameters are chosen for illustration purpose. The bi-linear shape is chosen because this is the shape most commonly used in FEM when delamination is included [4, 7, 34-37]. The value of the critical separation used in these simulations is much smaller than the value determined earlier from the experiments (here J_0 was about 3 mm), but is of the order of magnitude corresponding to the parameters describing the crack tip fracture energy. The *J* integral approach described in section 2 was applied to see if changing the Poisson's ratio or specimen width affected the calculated cohesive law. The aim of this preliminary investigation was to see if the cohesive law used in the model input can be determined from post processing the results of a delamination simulation, and what might affect the outcome. The end-opening displacement was extracted from the simulations for $(x_1, x_2) = (0, \pm H/2)$ and the resulting cohesive law was calculated using equation (4). First, a DCB specimen with the width of 30 mm was modelled with four different Poisson's ratios. Then the Poisson's ratio was fixed at 0.30 and the cohesive law was calculated from four models with different widths.

The calculated cohesive laws are plotted in Figure 5 a) and b). Both figures illustrate that the results are affected by both material properties and specimen geometry. The peak cohesive traction is significantly affected. Critical cohesive traction, as seen from the input cohesive law curve, is 20 MPa. Hence, all tractions above 20 MPa are in error. The reason tractions appear to exceed the critical cohesive traction is simply that the tractions are calculated based on the assumption that the crack tip opening displacement is equal across the width of the

sample. Due to the variation of stress state (and deformations) across the width of the beams, the crack will start to develop in the centre of the specimen before it is visible at the side of the specimen where the crack tip opening displacement is recorded. The calculated cohesive law is equal to the law used as model input when the Poisson's ratio is set to zero. The stress state is then reduced to plane stress throughout the specimen, with no anticlastic bending, and the crack front remains straight.

With respect to delamination problems, the effect of Poisson's ratio is thus very important for small separations corresponding to the part of the cohesive law that is associated with the crack tip fracture energy, J_0, which occurs in the range of separation of the order of tens of microns. The effect of the Poisson's ratio is likely to be much less significant for openings corresponding to the crack bridging regime, where the traction value is much lower and decreases to zero over an increase of 3 mm in the crack opening.

4.1 Fitting the cohesive law

In the following, we develop a cohesive law that incorporates the crack tip fracture energy, J_0. The cohesive law is modelled as multi-linear and an iterative approach is applied to determine the cohesive law parameters. First, a bridging law is calculated from equation (6). Then an area is added to the bridging law so that it becomes a complete cohesive law that includes the critical crack tip energy. The area added to the bridging law is based on the assumption that the interface behaviour is linearly elastic up to the critical interface strength. The shape presented in Figure 3 d) is chosen. By this approach J_0 will be dissipated within the shortest possible opening displacement without exceeding the assumed interface strength. At some opening displacement, δ_A^*, the crack tip energy is fully dissipated. The cohesive law should here include both the work of the bridging traction and the crack tip fracture energy J_0 at the end-opening δ_A^*. This point can be seen in Figure 3 d) where the Adjusted CL aligns with the Calculated BL. The area under the cohesive law at this point is (see equation (2))

$$J_{\mathrm{R,FPZ}}\left(\delta_A^*\right) = \int_0^{\delta_A^*} \sigma_{\mathrm{FB}}\left(\delta^*\right) \mathrm{d}\,\delta^* + J_0 \tag{7}$$

For openings larger than δ_A^*, the cohesive law should follow the bridging law, see Figure 3 d). However, in the present paper, the cohesive law is defined as a multi-linear law with linear interpolation between tractions defined for six opening displacements. The reason for using

such a multi-linear law is not based on a physical interpretation of the actual material behaviour, but rather the limitations of the constitutive model used for the numerical implementation [33].

Finally, the defined tractions and opening displacements are fitted to the experimental results using the optimisation tool LS-OPT [38]. The optimisation processes in LS-OPT are based on the response surface methodology [39]. The aim is to minimize the residual between a response from the model and a response from experimental test results. The opening displacement at the initial crack tip and the applied moments from the experimental results are used as objective for the optimization process. The response surface is created from a series of FEM simulations where the variables have been given different values. Upper and lower limits are defined for each variable, e.g. the opening displacement δ_4 has to have a value higher than δ_3 but lower than δ_5. The process of setting the values of the variables within the prescribed range is organised by the optimisation scheme used in LS-OPT. Here, an ASA hybrid optimization scheme with a D-optimal sampling procedure of linear order [38] is used. Each sampling point is produced from one FEM simulation of the complete delamination. One iteration includes a minimum number of sampling points defined by $i = 1.5(n+1)+1$, where i is the number of sampling points (complete finite element analyses of the entire test) and n is the number of variables. Each FEM simulation has a CPU time of 6-8 hours. The initial cohesive stiffness defined by δ_2 and σ_2 is chosen with respect to the finite thickness of the cohesive element and the stiffness of the bulk material. The traction plateau defined by σ_2 and σ_3 is kept flat by setting $\sigma_2 = \sigma_3$. To further reduce the number of variables, $\delta_5 = 0.5\ \delta_6$. The total number of variables is thus 6 and the number of sampling points therefore becomes 12.

The solution converged after seven iterations. The total CPU time for the optimisation process was approximately 550 hours. Figure 6 shows a selection of iteration results. The cohesive law parameters used as first guess (first sampling point in first iteration) are listed in Table 3, along with the resulting cohesive law after seven iterations. Both of the cohesive laws are plotted together with the measured bridging law in Figure 7. The cohesive law parameters with the greatest changes were δ_3 and σ_5.

A propagating delamination modelled using cohesive elements can have difficulties with convergence if the mesh is coarse [16]. In the present FE model the element dimensions in the plane of delamination were 0.5 x 0.5 mm, i.e. 30 elements across the modelled width of half the specimen. The fully developed failure process zone (FPZ) was more than 40 mm long and thus covered by more than 80 cohesive elements in the direction of crack propagation. The evolution of the crack tip, i.e. the development of J_0, was covered by approximately 5-10 elements as the crack propagated. The actual number of elements that cover the complete FPZ depends on the shape of the cohesive law. It is important to adjust the loading steps in the analysis so that the separation parameters describing the development of J_0 are captured. Figure 8 shows the distribution of normal opening traction in the cohesive elements used in the optimisation process as the delamination propagates towards the left. The crack tip does not follow a straight line through the width of the specimen. The plot illustrates that the crack opening displacement observed at the side of the specimen may not relate directly to the observed fracture resistance. It can be seen in Figure 8 that the interface tractions in the centre elements start to decrease from the critical traction level before the elements at the edge reach the critical traction level. In Table 3 it can be seen that the opening displacement (after fitting) is 0.001 mm when the cohesive tractions reaches 20 MPa and 0.013 mm when the tractions start to decrease. This indicates a difference in opening displacement across the width of at least 0.012 mm at a given position x_1.

LS-OPT was initially also used to do a sensitivity analysis. It was confirmed that the residual between the model and the experimental results was more sensitive to the changes in δ_3 than in $\sigma_{2,3}$. The traction was then given upper and lower bound values of 28 and 15 MPa, respectively. The reason for the choice of upper bound value is that the bulk material has a measured elastic limit at 28 MPa transverse to the fibre orientation [40]. The interface should be the weakest link for normal stresses in the thickness direction of the laminate and should therefore be lower than the damage threshold for the bulk material. The choice of lower limit was set to a low value based on the observed behaviour of the bulk material.

5 Evaluating the fitted cohesive law

Experimental results from standardised force-loaded double cantilever beam (DCB) delamination tests [18] were compared with numerical predictions based on the fitted cohesive law. The standardised test specimens were produced with the same constituents and procedures as the specimens for the moment based delamination tests. Loads were measured

with a load cell and the opening displacement at the end of the specimen was measured using an extensometer. However, an interpretation using linear-elastic fracture mechanics would be inappropriate due to large-scale bridging.

The numerical model had the same element dimensions as those used for modelling the moment based delamination tests. Implicit time integration with adaptive time step control was used. Material and geometrical properties are presented in Table 2. The FEM results based on the two cohesive laws, presented in Figure 7 and Table 3, are compared with the experimental DCB test results in Figure 9. It is clear that the cohesive law that was optimised using LS-OPT gives significantly better results than the multi-linear cohesive law used as a starting point for the optimisation.

6 Discussion

The success of the optimization process depends on the choices made during the optimization setup. The choice of sampling point selection scheme, number of sampling points and possible interaction between variables and optimization algorithm are choices that affect the computational cost of completing the necessary number of iterations. More important are the choices and assumptions made regarding the cohesive law. It is computationally favourable to choose few but well placed variables in the cohesive law and keep as many properties as possible constant. The number of simulations per iteration is governed by the sampling selection scheme used and the number of variables evaluated. Adding an additional variable can cause the number of simulations per iteration to increase significantly. It is therefore important to have an approximate idea of what the actual cohesive law should look like and use as few variables as possible. If the initial value is chosen poorly, it may be difficult for the optimization process to produce acceptable results within reasonable computational costs.

The need for adjusting the multi-linear cohesive law based on the *J* integral approach can be seen in Figure 6. The *J* integral approach implicitly assumes the crack opening is the same across the width of the specimen. A 3D FE model will include the anticlastic bending effects and the associated variations in stress state and crack opening across the width. A cohesive law that is determined based on plane assumptions will then fail to capture the response from the experiment when used in a 3D FE model. This is the reason why the blue curve in Figure 6 is very different from the experimental results.

The choice of using a multi-linear shape for the cohesive law is based on the limitations of the constitutive model used in the finite element implementation. The reason for defining only six points on the multi-linear cohesive law is found in the optimisation process. Every sampling point is based on the result of a complete FEM simulation of the DCB test. Each FEM simulation has a CPU-time of approximately 6-8 CPU hours. Increasing the number of variables therefore significantly increases the CPU time of the total optimisation procedure. The number of sampling points used here was 12 and acceptable results were found after 7 iterations. The total CPU time for the optimisation process was approximately 550 hours.

In Figure 9, the resulting fitted cohesive law produced significantly better results than the multi-linear cohesive law used as a starting point for the optimisation procedure. However, neither of the simulated models completely captured the stiffness shown by the experimental results. The simulated stiffness is in both cases higher than that of the experimental result. The discrepancy is partially attributed to the compliance of the test fixture and is considered acceptable since the beams are modelled with the same isotropic material model as used for the DCB samples. The resin, fabric, sizing, curing procedure and fibre volume fraction are equal for both types of DCB samples. In Figure 9 a plateau is observed in the applied load at an opening of about 7-8 mm on the FEM results from the fitted cohesive law. This may have been caused by the restrictions made on the variables during the optimisation setup. The drop in interface stiffness going from the crack-tip dominated region to the fibre bridging dominated region of the cohesive law might be too steep. Dissipating the crack tip energy within a short opening displacement (i.e. a high peak stress over a small opening), still seems to be an appropriate approach without causing numerical instability.

The initial stiffness of the cohesive law should be chosen with respect to the thickness of the cohesive elements so that the traction-separation relation of a finite-thickness element resembles the stress-strain relations of the bulk material. If the stiffness is chosen poorly the overall bending response of the laminate may be affected and become too soft. Another challenge is that rapidly changing stiffness in the cohesive elements may cause numerical instability. Reducing the size of the cohesive elements reduces the rate of change in stiffness in adjacent elements in the direction of the propagating delamination. Reducing the time step will of course also reduce the rate of change in stiffness. If the load step in an implicit model is sufficiently small, an explicit solution might be faster even if the load steps then will be significantly smaller.

The varying stress state and crack opening across the width of the specimen (induced by the Poisson effects) is not taken into account in the experimental J integral approach, eq. (4). The effects presented in Figure 5 a) and b) show the tendency of over-estimating the tractions of the cohesive law at small opening displacement, and underestimating them at larger opening displacements. But the total areas of the cohesive laws are all equal to the steady state fracture resistance. The stress variations across the width seem to give the impression of more rapid energy dissipation if evaluated from the opening displacement measured at the side of the specimen. This is also apparent from the fracture resistance curves from the simulations in Figure 6. The cohesive tractions associated with crack bridging vary much more slowly over much larger separations and are not expected to be significantly influenced by the Poisson effects.

In the experiments, there were some minor discrepancies between initiation of crack end opening and the first acoustic events. If the crack-end opening displacement first initiates at the half width across the specimen before it initiates at the side of the specimen, the first acoustic events should be detected before any crack-end opening displacement is observed at the side of the specimen.

The presence of anticlastic bending and the effect it has on the relation between fracture resistance and crack tip opening at small opening displacement might affect the observed value of the critical crack tip energy, J_0. The findings presented in this paper suggest that beams displaying anticlastic bending might give the appearance of having higher values of J_0 than beams with little anticlastic bending. The reason for this apparent higher value of J_0 is the delayed opening of the crack at the sides of the specimen where the crack tip opening displacement used to evaluate J_0 is measured. This effect could be investigated by checking if the observed value of J_0 changes with increasing specimen width.

For materials where the cohesive tractions vary rapidly over small openings it would be convenient to have a correction function that could account for the effect of having states of stress and deformation that change across the width of the specimen. A challenge with such a function is that the difference between measured and actual cohesive law is dependent on the shape of the actual cohesive law. With this in mind, inverse modelling using the three-step optimisation scheme presented here seems currently to be the most promising approach. The

effects of Poisson's ratio on the beam deformation (in the form of anticlastic bending) can be reduced by increasing the beam height relative to the beam width (increasing H/B) - going from a plate-like geometry toward a more beam-like geometry. This will not eliminate the presence of anticlastic bending, but it will make the measurements of the opening displacements at the side of the specimen closer to the value in the middle of the specimens, thus making them more relevant for the overall behaviour.

7 Concluding remarks

The object of this study was to show that a cohesive law associated with the crack tip fracture energy could be obtained from experimental tests for implementation in 3D finite element models. A procedure to achieve this has been developed and tested. Such a cohesive law for large scale bridging problems consists of two distinct energy-dissipating phenomena: crack tip energy and fibre bridging. A bridging law describing the fibre bridging is calculated from the fracture resistance curve by applying the path independent J integral approach for plane stress. An approximate multi-linear cohesive law is then obtained by combining tractions and opening displacements for dissipation of fracture energy within a small opening displacement, corresponding to the crack tip fracture energy, J_0, and a simplified bridging law that operates over larger openings. The parameters of the multi-linear cohesive law are then fitted to account for the changing stress state through the width of the test specimen by using the optimisation tool LS-OPT. The fitted cohesive law is evaluated by comparing FEM and experimental results for a series of ASTM D 5528 Mode I delamination tests. The FEM result using the fitted cohesive law is found to agree well with the response observed in the experimental tests. The three-step procedure presented here is successfully shown to characterize a Mode I cohesive law. The changing state of stress and deformation across the width of the specimen is affected by both material properties (Poisson's ratio) and the geometry of the test specimen. This three dimensional effect is a significant source of error for small cohesive openings and needs to be taken into account when determining a cohesive law from the fracture resistance, in particular the traction for small separations corresponding to the crack tip fracture energy. The effect is expected to be small for problems where the cohesive tractions represent large-scale bridging for which the tractions are low and decrease slowly to zero over several millimetres.

Acknowledgements

This work is part of the collaborative project "Composite structures under impact loading" with the industrial partners Flowtite Technology AS, Nammo Raufoss AS, Ragasco AS and the research institutes Norwegian University of Science and Technology (NTNU), University of Oslo (UiO), SINTEF Materials and Chemistry and SINTEF Raufoss Manufacturing. The authors would like to express their thanks for the financial support by the Norwegian Research Council (grant 193238/i40) and the industrial partners. The authors would also like to thank all partners in the project for constructive discussions. The fourth author was supported by the Danish Centre for Composite Structures and Materials for Wind Turbines (DCCSM), grant no. 09-067212 from the Danish Strategic Research Council. The cooperation between SINTEF and Technical University of Denmark, Department of Wind Energy was partly funded by the Norwegian Research Centre for Offshore Wind Technology (NOWITECH).

References

[1] Barenblatt GI. The Mathematical Theory of Equilibrium Cracks in Brittle Fracture. Advances in Applied Mechanics, vol. Volume 7: Elsevier; 1962. p. 55-129.
[2] Dugdale DS. Yielding of steel sheets containing slits. Journal of the Mechanics and Physics of Solids. 1960;8(2):100-104.
[3] Geubelle PH, Baylor JS. Impact-induced delamination of composites: a 2D simulation. Composites Part B: Engineering. 1998;29(5):589-602.
[4] Borg R, Nilsson L, Simonsson K. Simulation of delamination in fiber composites with a discrete cohesive failure model. Composites Science and Technology. 2001;61(5):667-677.
[5] Borg R, Nilsson L, Simonsson K. Modeling of delamination using a discretized cohesive zone and damage formulation. Composites Science and Technology. 2002;62(10–11):1299-1314.
[6] Borg R, Nilsson L, Simonsson K. Simulating DCB, ENF and MMB experiments using shell elements and a cohesive zone model. Composites Science and Technology. 2004;64(2):269-278.
[7] Elmarakbi AM, Hu N, Fukunaga H. Finite element simulation of delamination growth in composite materials using LS-DYNA. Composites Science and Technology. 2009;69(14):2383-2391.
[8] Harper PW, Hallett SR. Cohesive zone length in numerical simulations of composite delamination. Engineering Fracture Mechanics. 2008;75(16):4774-4792.
[9] Harper PW, Sun L, Hallett SR. A study on the influence of cohesive zone interface element strength parameters on mixed mode behaviour. Composites Part A: Applied Science and Manufacturing. 2012;43(4):722-734.
[10] Hu N, Zemba Y, Okabe T, Yan C, Fukunaga H, Elmarakbi AM. A new cohesive model for simulating delamination propagation in composite laminates under transverse loads. Mechanics of Materials. 2008;40(11):920-935.
[11] Liu PF, Islam MM. A nonlinear cohesive model for mixed-mode delamination of composite laminates. Composite Structures. 2013;106(0):47-56.

[12] Sørensen BF, Jacobsen TK. Determination of cohesive laws by the J integral approach. Engineering Fracture Mechanics. 2003;70(14):1841-1858.
[13] Sørensen BF, Jacobsen TK. Characterizing delamination of fibre composites by mixed mode cohesive laws. Composites Science and Technology. 2009;69:445-456.
[14] Sørensen BF, Kirkegaard P. Determination of mixed mode cohesive laws. Engineering Fracture Mechanics. 2006;73(17):2642-2661.
[15] Turon A, Camanho PP, Costa J, Renart J. Accurate simulation of delamination growth under mixed-mode loading using cohesive elements: Definition of interlaminar strengths and elastic stiffness. Composite Structures. 2010;92(8):1857-1864.
[16] Turon A, Dávila CG, Camanho PP, Costa J. An engineering solution for mesh size effects in the simulation of delamination using cohesive zone models. Engineering Fracture Mechanics. 2007;74(10):1665-1682.
[17] Sørensen BF, Jørgensen K, Jacobsen TK, Østergaard RC. DCB-specimen loaded with uneven bending moments. International Journal of Fracture. 2006(141):163–176.
[18] ASTM. Standard Test Method for Mode I Interlaminar Fracture Toughness of Unidirectional Fiber-Reinforced Polymer Matrix Composites. vol. D5528–01 (Reapproved 2007): ASTM International; 2009.
[19] ASTM. Standard Test Method for Mixed Mode I-Mode II Interlaminar Fracture Toughness of Unidirectional Fiber Reinforced Polymer Matrix Composites. vol. D6671/D6671M–06: ASTM International; 2009.
[20] Rice JR. A Path Independent Integral and the Approximate Analysis of Strain Concentration by Notches and Cracks. Journal of Applied Mechanics. 1968;35(2):379-386.
[21] Bao G, Ho S, Suo Z, Fan B. The role of material orthotropy in fracture specimens for composites. International Journal of Solids and Structures. 1992;29(9):1105-1116.
[22] McGugan M, Pereira G, Sørensen BF, Toftegaard H, Branner K. Damage tolerance and structural monitoring for wind turbine blades. Philosophical Transactions of the Royal Society A. 2015;373(2035).
[23] Li VC, Ward RJ. A novel testing technique for post-peak tensile behaviour of cementitious materials. In: Mihashi H, Takahashi H, Wittmann FH, editors. Fracture toughness and fracture energy – testing methods for concrete and rocks, Rotterdam A.A. Balkema Publishers; 1989. p. 183–195.
[24] Olsson P, Stigh U. On the determination of the constitutive properties of thin interphase layers - An exact inverse solution. International Journal of Fracture. 1989;41(4):R71-R76.
[25] Anthony J, Paris P. Instantaneous evaluation of J and C. International Journal of Fracture. 1988;38(1):R19-R21.
[26] Megson THG. Ch 9 - Bending of Beams. Structural and Stress Analysis. 3 ed: Elsivier; 2014.
[27] Tarantola A. Inverse Problem Theory and methods for model parameter estimation. Philadelphia: Society for Industiral and Applied Mathematics; 2005.
[28] Yang QD, Thouless MD, Ward SM. Numerical simulations of adhesively-bonded beams failing with extensive plastic deformation. Journal of the Mechanics and Physics of Solids. 1999;47(6):1337-1353.
[29] Mohammed I, Liechti KM. Cohesive zone modeling of crack nucleation at bimaterial corners. Journal of the Mechanics and Physics of Solids. 2000;48(4):735-764.
[30] Yang QD, Thouless MD. Mixed-mode fracture analyses of plastically-deforming adhesive joints. International Journal of Fracture. 2001;110(2):175-187.
[31] Suo Z, Bao G, Fan B. Delamination R-curve phenomena due to damage. Journal of the Mechanics and Physics of Solids. 1992;40(1):1-16.

[32] Kotousov A, Lazzarin P, Berto F, Harding S. Effect of the thickness on elastic deformation and quasi-brittle fracture of plate components. Engineering Fracture Mechanics. 2010;77(11):1665-1681.
[33] LS-DYNA Keyword User's Manuals Volume 1 Version 971. Livermore Software Technology Corporation 2007.
[34] Dantuluri V, Maiti S, Geubelle PH, Patel R, Kilic H. Cohesive modeling of delamination in Z-pin reinforced composite laminates. Composites Science and Technology. 2007;67(3–4):616-631.
[35] Xie D, Salvi AG, Sun C, Waas AM, Caliskan A. Discrete Cohesive Zone Model to Simulate Static Fracture in 2D Triaxially Braided Carbon Fiber Composites. Journal of Composite Materials. 2006;40(22):2025-2046.
[36] Camanho PP, Davila CG, de Moura MF. Numerical Simulation of Mixed-Mode Progressive Delamination in Composite Materials. Journal of Composite Materials. 2003;37(16):1415-1438.
[37] Mollón V, Bonhomme J, Elmarakbi AM, Argüelles A, Viña J. Finite element modelling of mode I delamination specimens by means of implicit and explicit solvers. Polymer Testing. 2012;31(3):404-410.
[38] LS-OPT User's Manual Version 4.2 LIVERMORE SOFTWARE TECHNOLOGY CORPORATION2012.
[39] Myers RH, Montgomery DC. Response Surface Methodology. Process and Product Optimization
using Designed Experiments.: Wiley; 1995.
[40] Joki RK, Grytten F, Hayman B. Nonlinear response in glass fibre non-crimp fabric reinforced vinylester composites. Composites Part B: Engineering. 2015;77(0):105-111.

Table 1. Material and geometric properties for moment loaded DCB specimen.

B	30.11	mm	Width
$2H$	17.40	mm	Thickness
l	300	mm	Length
a_0	59	mm	Initial delamination
E	37	GPa	Flexural modulus
ν_{12}	0.29		Poisson's ratio
S_{22}=S_{33}	28	MPa	Transverse ply strength
σ_{Ic}	20	MPa	Mode I Critical interface strength
δ_0	3	mm	Mode I Critical opening displacement
J_{ss}	1	kJ/m^2	Mode I Steady state fracture resistance
J_0	0.21	kJ/m^2	Mode I crack tip fracture energy
J_a	0.33	kJ/m^2	Fitting parameter for equation (5)
J_b	0.67	kJ/m^2	Fitting parameter for equation (5)
δ_a	6.67	mm	Fitting parameter for equation (5)
δ_b	0.65	mm	Fitting parameter for equation (5)

Table 2. Geometric properties for standardised DCB specimen.

W	22	mm	Width
$2H$	4.0	mm	Thickness
l	150	mm	Length
a_0	50	mm	Initial delamination

Table 3. Cohesive law parameters before and after fitting.

Before fitting				After fitting			
[mm]		[MPa]		[mm]		[MPa]	
$\delta_1 =$	0.00	$\sigma_1 =$	0.00	$\delta_1 =$	0.00	$\sigma_1 =$	0.00
$\delta_2 =$	0.0010	$\sigma_2 =$	20.00	$\delta_2 =$	0.0010	$\sigma_2 =$	20.00
$\delta_3 =$	0.0296	$\sigma_3 =$	20.00	$\delta_3 =$	0.0130	$\sigma_3 =$	20.00
$\delta_4 =$	0.0326	$\sigma_4 =$	0.4000	$\delta_4 =$	0.0181	$\sigma_4 =$	0.6200
$\delta_5 =$	1.5088	$\sigma_5 =$	0.0800	$\delta_5 =$	1.5088	$\sigma_5 =$	0.1568
$\delta_6 =$	3.0176	$\sigma_6 =$	0.00	$\delta_6 =$	3.0176	$\sigma_6 =$	0.00

Figure 1. Integration path for the *J* integral: a) integration path locally around the cohesive zone, b) interpretation of traction vs. separation in the FPZ, and c) the integration path along the external boundaries of a DCB specimen loaded with pure bending moments.

Figure 2. Geometry of DCB specimens.

Figure 3. Fracture resistance response from a DCB specimen loaded with pure bending moments. Fracture resistance and cohesive traction are shown as a function of normalized separation (normalized by $\delta_0 = 3$ mm). Fitted function on top of experimental scatter a) and b). Details of the calculated bridging law (BL) c) and the adjusted cohesive law (CL) (adjusted for small separations only) - note different scales on the axis d).

Figure 4. The FEM model of the DCB specimen for the moment based delamination test.

Figure 5. Comparing a bi-linear cohesive law used in the FE model and the cohesive law (CL) calculated after post processing the model after a) changing the Poison's ratio, and b) changing the specimen width.

Figure 6. Fracture resistance during iterative fitting of cohesive law compared to experimental test result used as fitting objective.

Figure 7. a) The calculated bridging law with the cohesive law before (blue colour) and after fitting (green colour). The details of the crack tip relations are presented in b), and the details of the fibre bridging region is presented in c).

Figure 8. Contour plot illustrating opening tractions in cohesive elements as crack propagates. Several cohesive elements were deleted after exceeding critical separation in the lower two plots. The total active cohesive zone length, L, is indicated in the lower two plots. The indicated zone covered by eight elements represents the crack tip zone.

Figure 9. FEM result before and after fitting of cohesive law compared to experimental results.

Figure 1

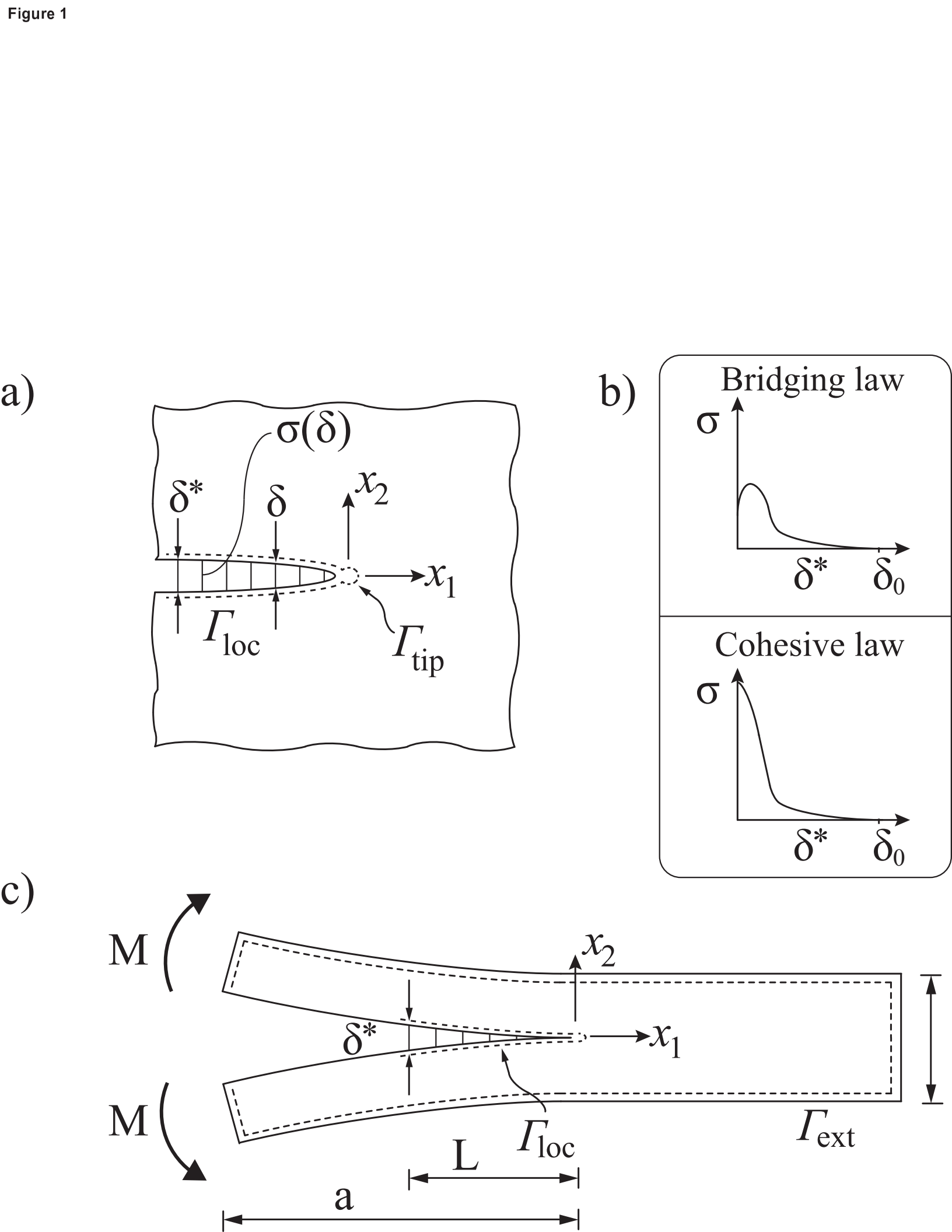
a)
σ(δ)
δ*
δ
x2
x1
Γloc
Γtip
b)
Bridging law
σ
δ*
δ0
Cohesive law
σ
δ*
δ0
c)
M
M
x2
x1
δ*
Γloc
Γext
L
a

Figure 2
Click here to download high resolution image

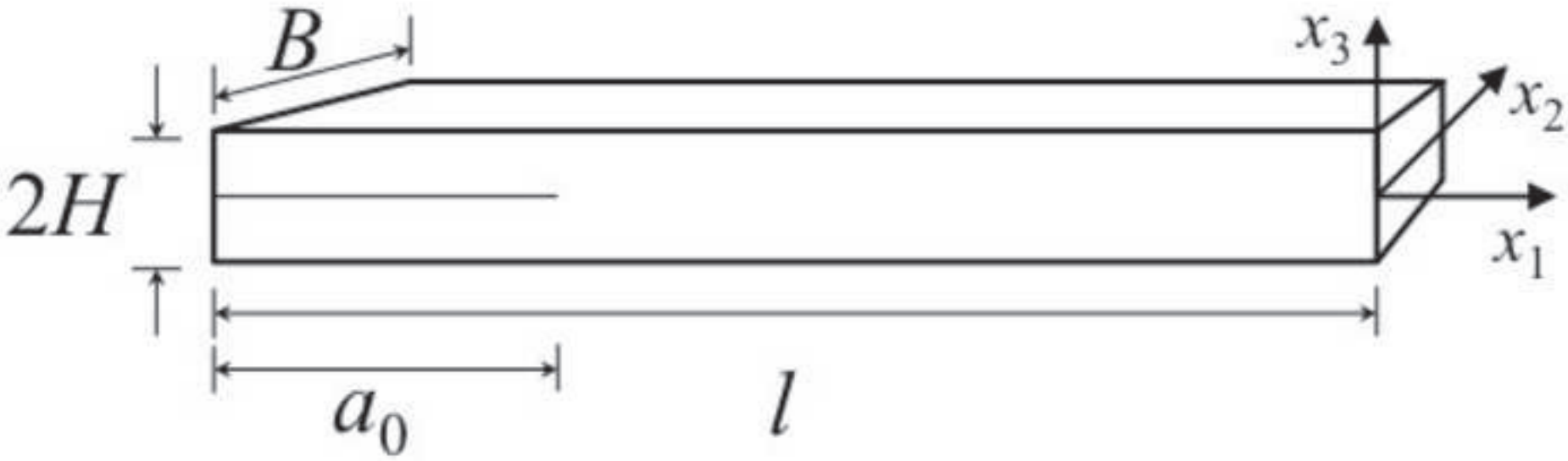

Figure 3
Click here to download high resolution image

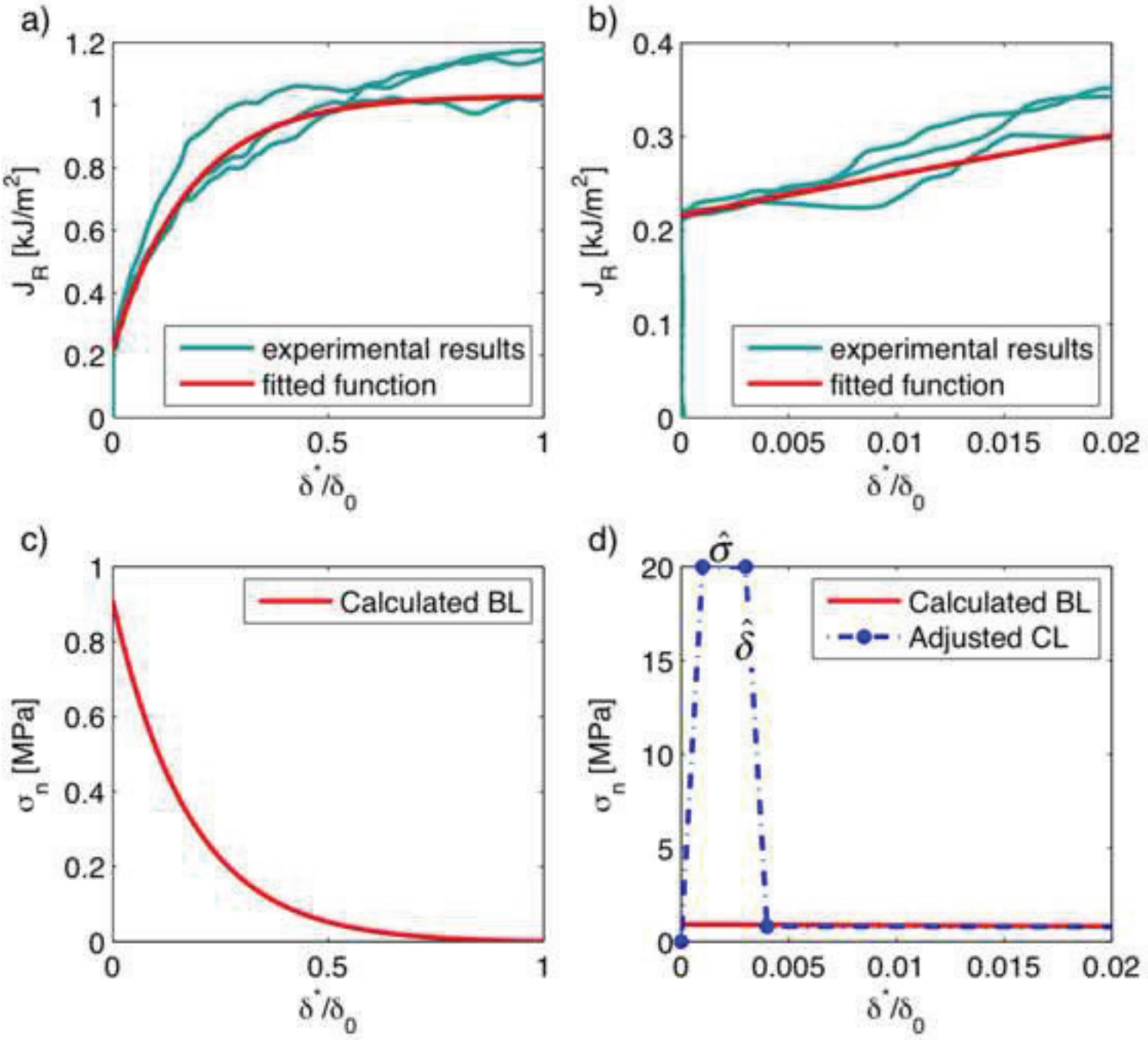

Figure 4
Click here to download high resolution image

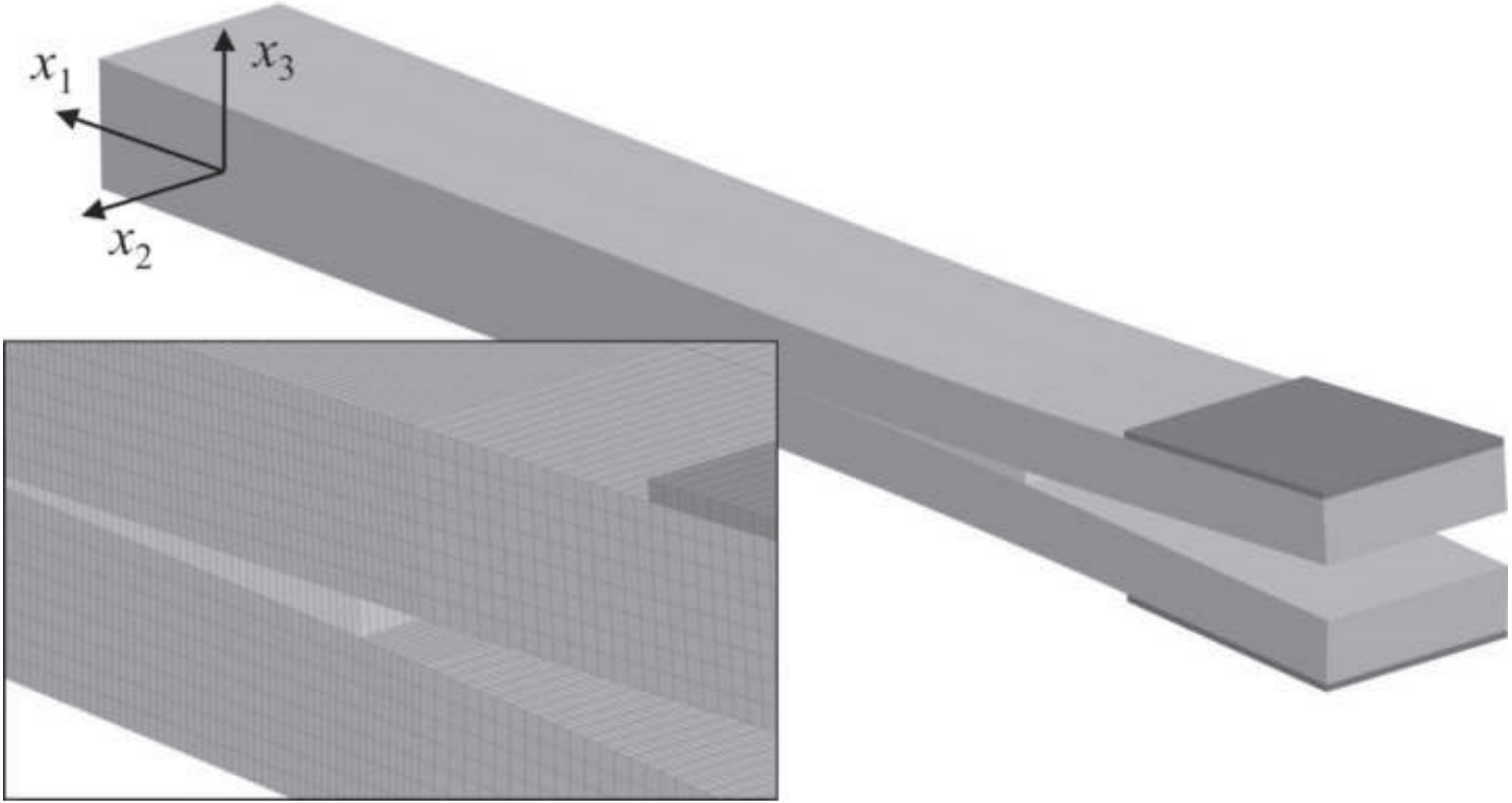

Figure 5

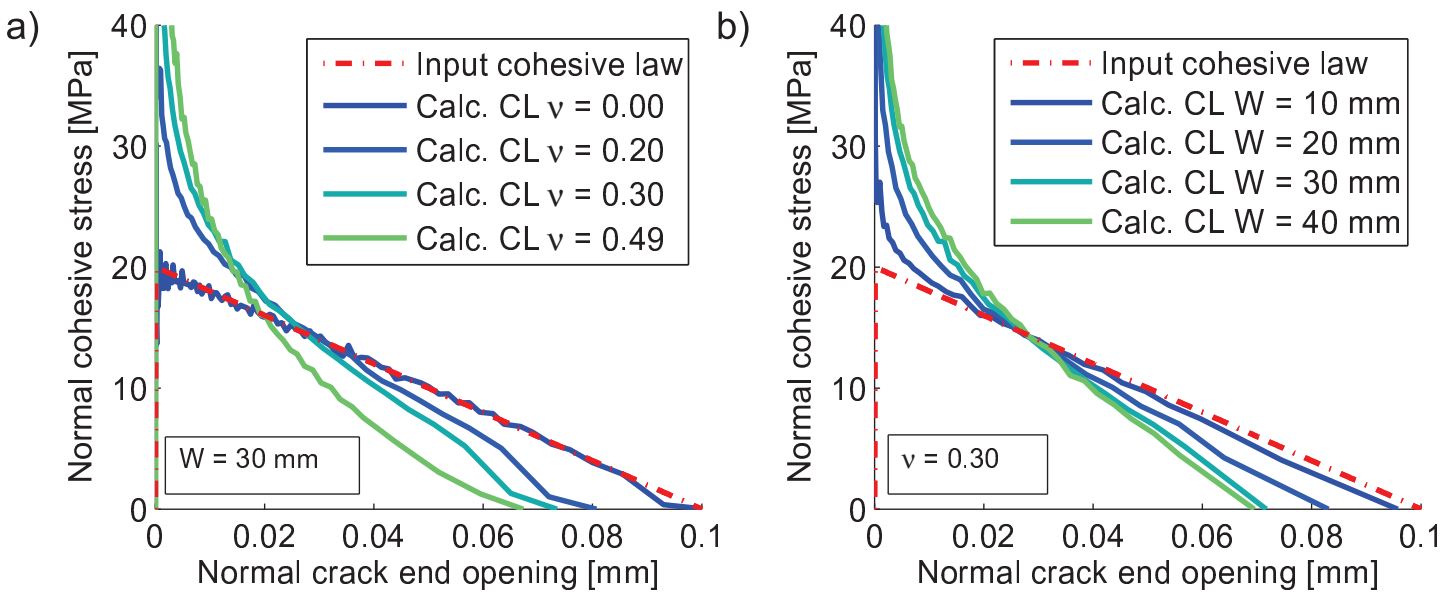
a)
Normal cohesive stress [MPa]
Normal crack end opening [mm]
Input cohesive law
Calc. CL ν = 0.00
Calc. CL ν = 0.20
Calc. CL ν = 0.30
Calc. CL ν = 0.49
W = 30 mm
b)
Normal cohesive stress [MPa]
Normal crack end opening [mm]
Input cohesive law
Calc. CL W = 10 mm
Calc. CL W = 20 mm
Calc. CL W = 30 mm
Calc. CL W = 40 mm
ν = 0.30

Figure 6

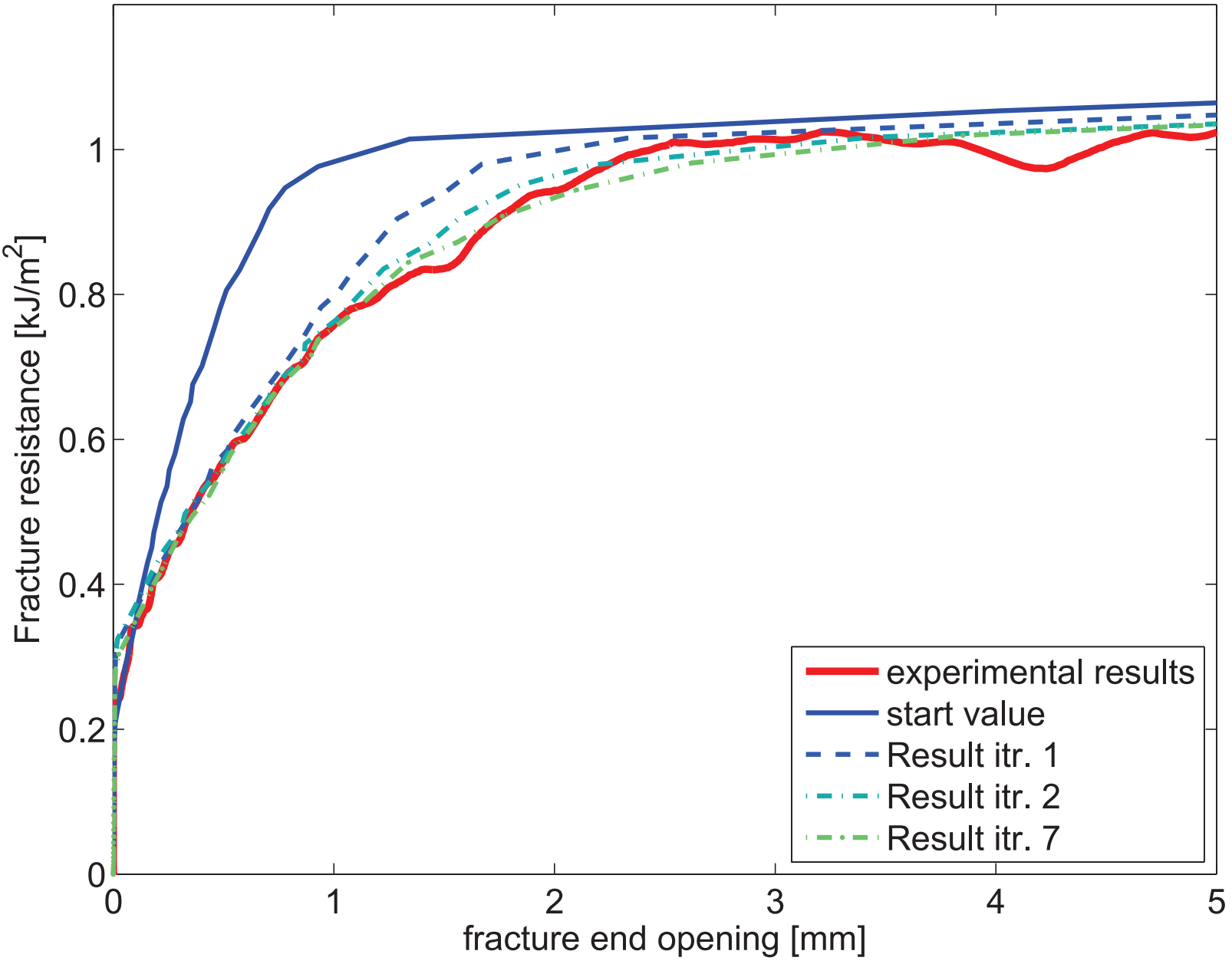
Fracture resistance [kJ/m^2]
fracture end opening [mm]
0
0.2
0.4
0.6
0.8
1
0
1
2
3
4
5
experimental results
start value
Result itr. 1
Result itr. 2
Result itr. 7

Figure 7
Click here to download high resolution image

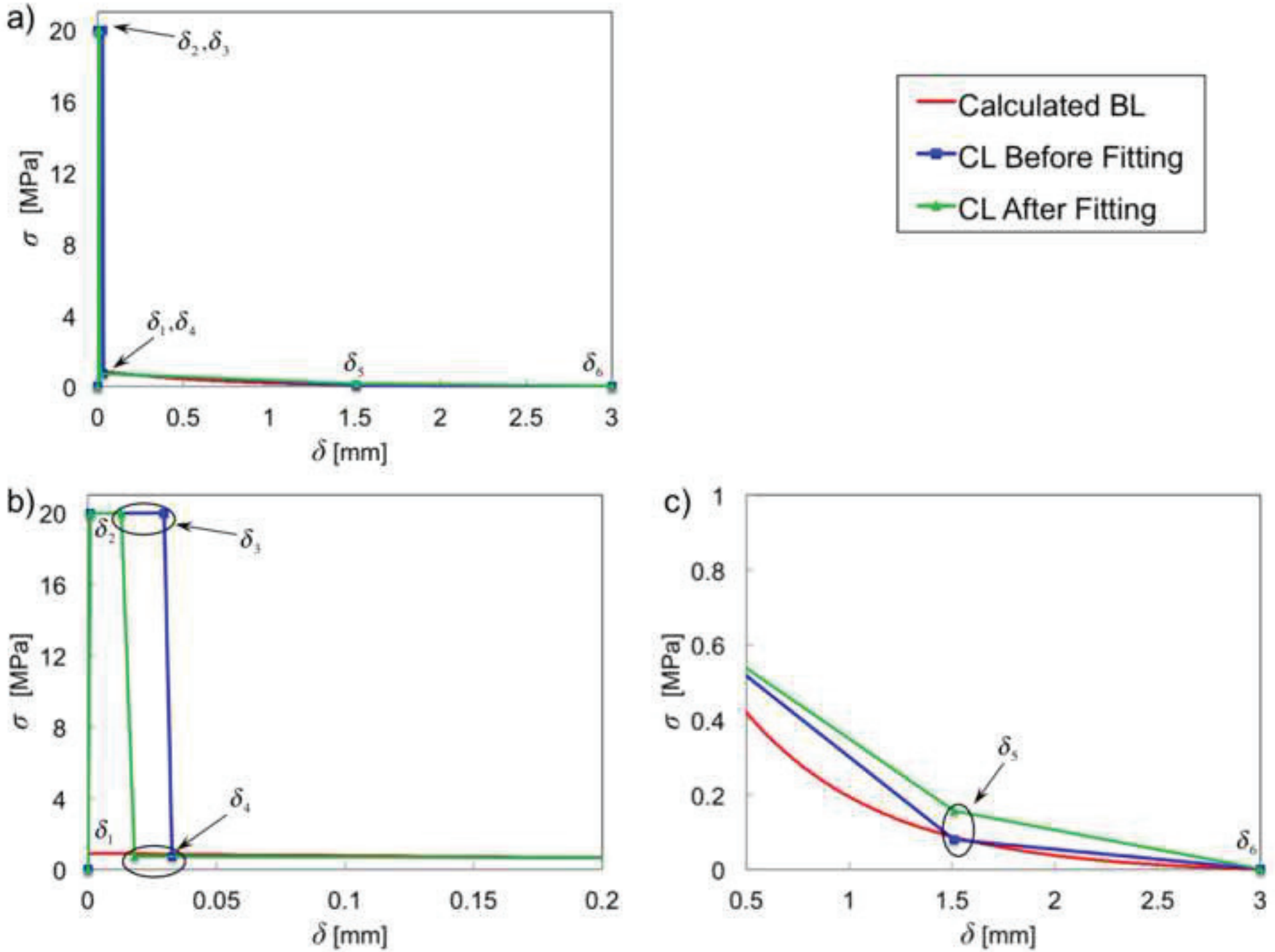

Figure 8
Click here to download high resolution image

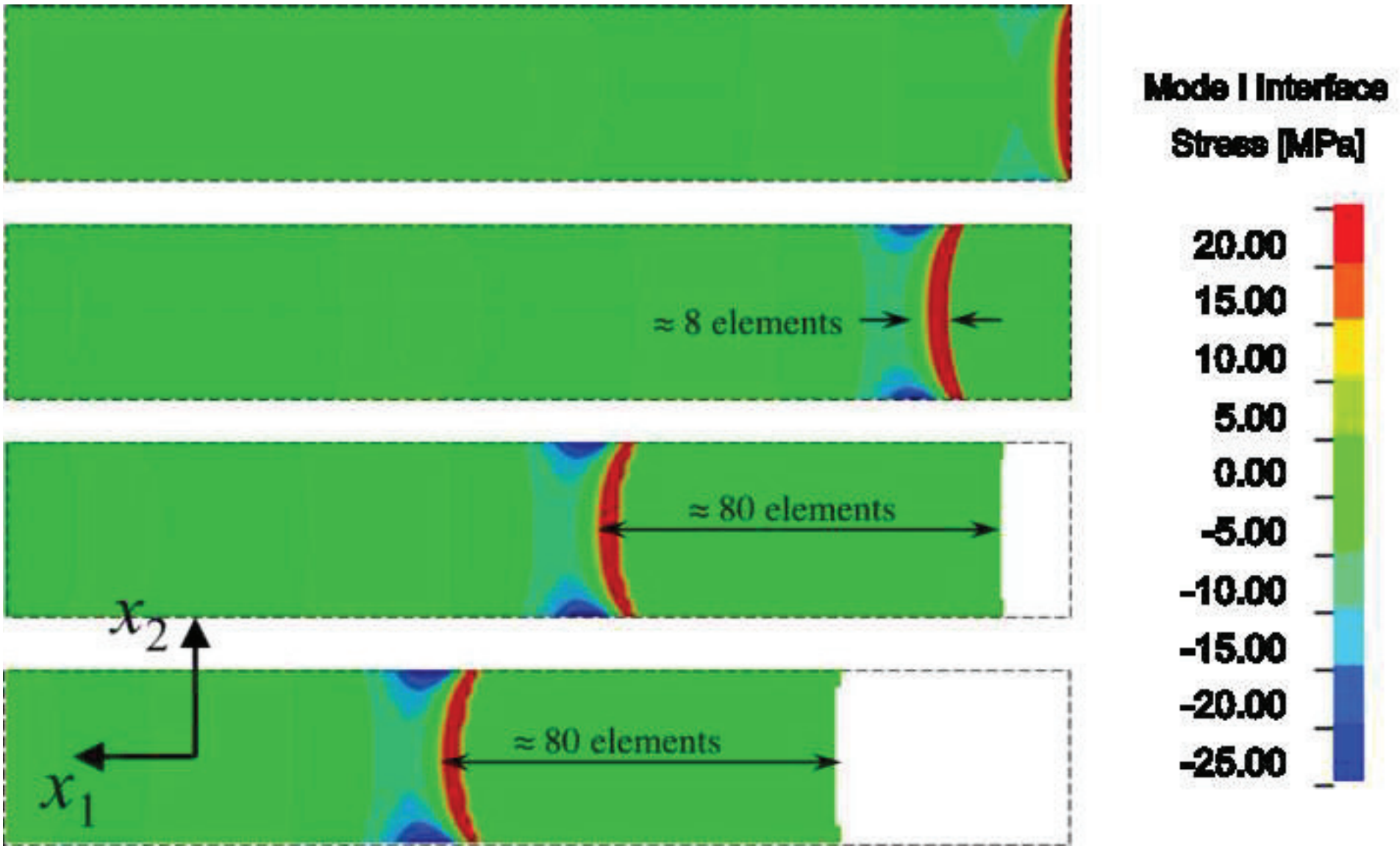

Figure 9
Click here to download high resolution image